Supporting Information for

Integration of Hydrogen Evolution Reaction and Microplasma Induced Vapor Generation: A Strategy for Improving Safety and Sensitivity of Microplasma Optical Emission Spectrometry

Yubin Su,[a] Xiaomin Pan,[a] Yao Lin,[b] Yurong Deng[a], and Chengbin Zheng [a,*]

[a] Key Laboratory of Green Chemistry & Technology of MOE, College of Chemistry, Sichuan University, Chengdu 610064, P. R. China

[b] Pen-Tung Sah Institute of Micro-Nano Science & Technology, Xiamen University, Xiamen 361005, P. R. China

[*]Corresponding author: abinscu@scu.edu.cn (C. B. Zheng)

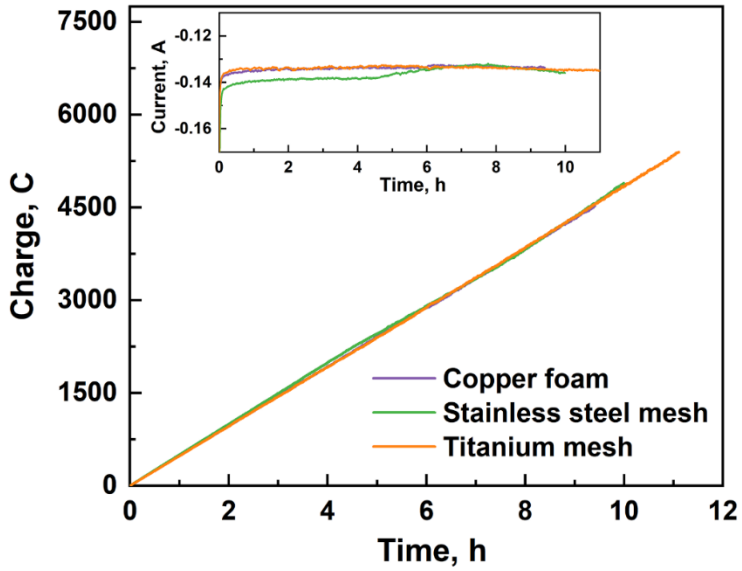

Figure. S1. Long-term controlled potential electrolysis of Co-P nanomaterials in 1 M KOH at an overpotential of −4 V (Inset: the corresponding current change over time of Co-P nanomaterials during the electrolysis).

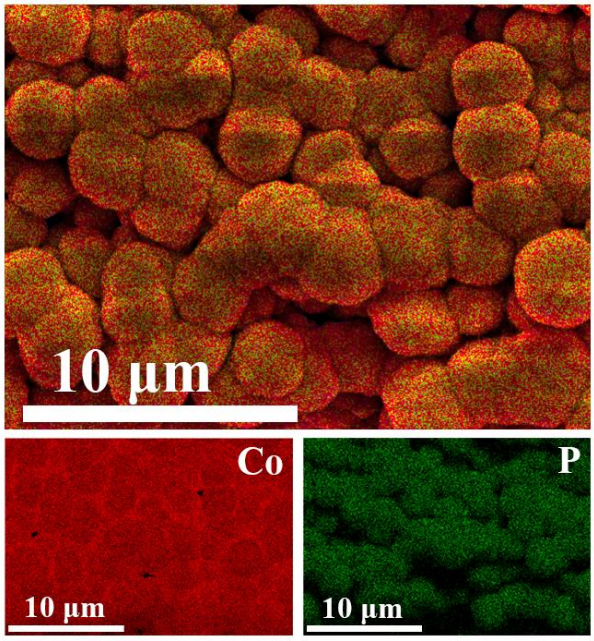

Figure. S2. Elemental mapping of Co and P in the Co-P nanomaterials on titanium mesh.

XRD results of the Co-P/Ti:

To understand the crystalline structure of the generated Co-P nanomaterials, the Co-P/Ti nanomaterials were further characterized by XRD. As shown in Fig. S3, diffraction peaks of Co are observed at 41.7°, 44.8°, 47.6°, 62.7°, and 75.9°, corresponding to (100), (002), (101), (102), and (110) crystal plane, whereas no other obvious P-containing diffraction peaks were observed. The diffraction peak of Ti (from the titanium mesh substrate) is consistent with the standard diffraction pattern JCPDS no. 44-1294, indicating that the prepared Co-P/Ti contains crystalline Co while P is present in an amorphous form, which is consistent with previous reports.[1, 2]

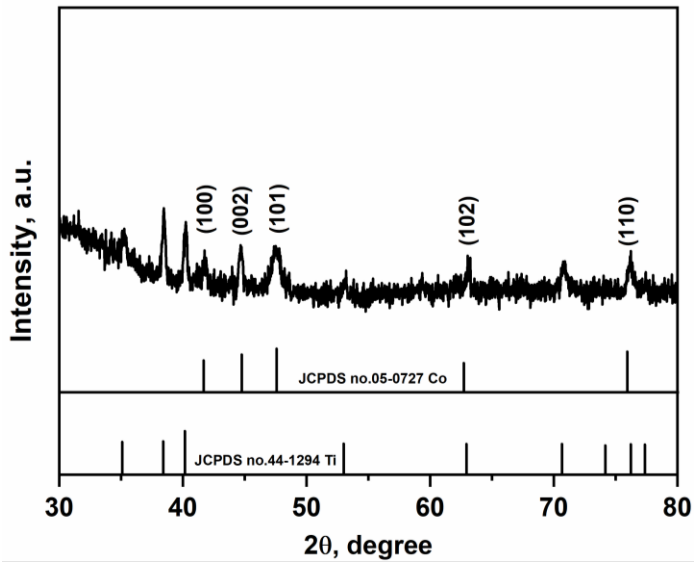

Figure. S3. XRD pattern of the Co-P/Ti.

XPS results of the Co-P/Ti:

XPS was used to further analyze the composition and chemical valence of each element in the Co-P/Ti nanomaterials. As shown in Fig. S4, the characteristic peaks associated with Co and P can be observed. Two distinct characteristic peaks can be observed in the Co 2p XPS spectrum (Fig. S5a), in which 778.1 and 793.2 eV are close to the binding energy of Co $2p_{3/2}$ and Co $2p_{1/2}$, respectively.[1, 3, 4] The cobalt phosphide obtained by electrodeposition is connected with covalent bonds between cobalt and phosphorus rather than ionic bonds, thus making the characteristic peaks in cobalt phosphide and cobalt monomer very close to each other and forming a mixed peak. Consequently, the characteristic peaks of 778.1 and 793.2 eV can be attributed to cobalt monomer as well as cobalt phosphide.[3] The other peaks like binding energies of 781.0 and 796.9 eV can be attributed to the characteristic peaks of Co_3O_4 formed by oxidation on the material surface due to exposure to air.[5] As present in Fig. S5b, two characteristic peaks corresponding to P $2p_{1/2}$ and P $2p_{3/2}$ are observed in the P 2p region with binding energies of about 130.6 and 129.7 eV, respectively. Additionally, there is an obvious characteristic peak of phosphate at the binding energy of about 133.6 eV, which is caused by air oxidation.[6] It can be concluded that in addition to cobalt phosphide, the components of the prepared Co-P/Ti nanomaterials also contain cobalt and cobalt tetroxide, which are consistent with previous reports.[1, 2]

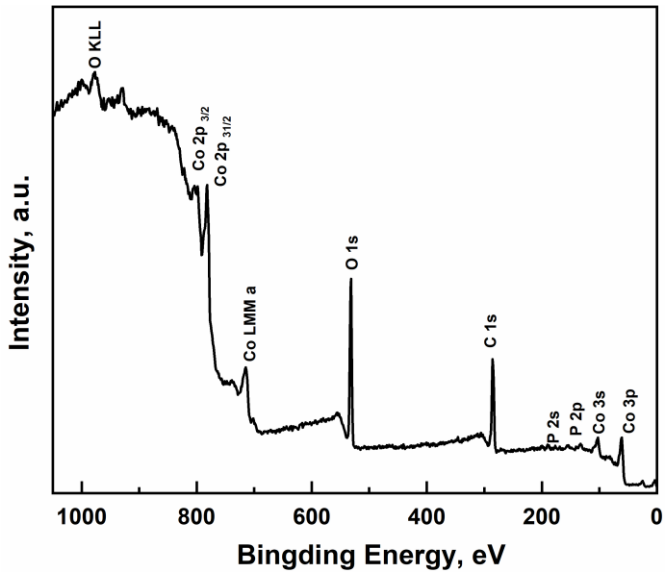

Figure. S4. XPS spectrum of the Co-P/Ti.

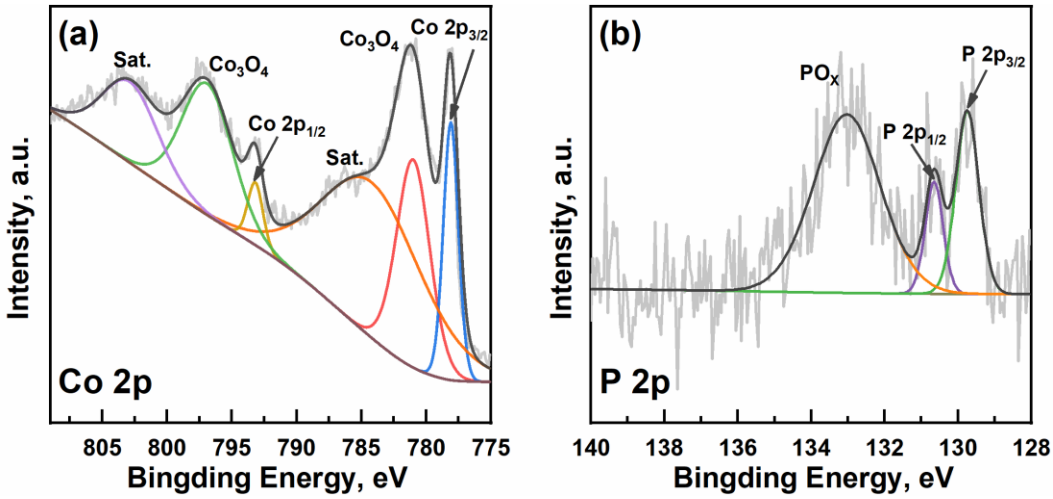

Figure. S5. XPS spectrum of the Co-P/Ti: Co 2p region (a) and P 2p region (b).

Optimization of experimental parameters for HER-LED-μPIVG-μPD-OES:

The vapor generation products of Cd and Zn are generally considered to be CdH_2 or ZnH_2, thus the amount of H_2 is crucial for their μPIVG efficiencies.[7-9] The amount of H_2 is directly related to the applied voltage of HER in the proposed method, hence the effect of HER voltage on the response of Hg, Cd, and Zn was investigated. As shown in Fig. S6a, the relative peak area of Cd and Zn gradually increased with the increase of HER voltage and slightly decreased after reaching –5 V. Although the relative peak area of Hg does not show much change at the beginning with the increase of voltage, it is suppressed after –4 V. Suppression of the relative peak area of Hg, Cd, and Zn at high voltages may be because excess hydrogen produced by HER dilutes the analytes and destabilizes the microplasma. To achieve the simultaneous detection of the three elements, a full electrolytic voltage of –4 V was therefore chosen for the subsequent experiments.

The sample flow rate affects the efficiency of sample transport and further affects the efficiency of μPIVG, thus the effect of sample flow rate was investigated. As shown in Fig. S6b, the peak area of Hg, Cd, and Zn gradually decreased with the increase of sample flow rate owing to the dilution of analytes. However, a low sample flow rate reduced efficiency of sample transport and resulted in peak trailing, which is consistent with previous report.[10] Therefore, a sample flow rate of 2 mL min^{-1} was thus selected for subsequent experiments to ensure the sample transport efficiency and μPIVG efficiency of Hg, Cd, and Zn at the same time.

Ar not only serves as carrier gas to transport vapor to PD-OES, but also acts as the discharge gas to maintain microplasma. Fig. S6c shows the variation trend of relative peak area with Ar flow rate, which indicates that the maximum response of Hg, Cd, and Zn was obtained at 75, 100, and 150 mL min^{-1}, respectively. Low Ar flow rate reduces the transport efficiencies of analytes, whereas a higher flow rate may result in significant dilution of analytes in the carrier gas and reduce the residence time in the excitation source. A 100 mL min^{-1} flow rate of Ar was thus selected for the subsequent experiments in simultaneous consideration of the maximum response of Hg, Cd, and Zn.

The effect of the discharge voltage of LED on the responses of Hg, Cd, and Zn was investigated. The results are summarized in Fig. S6d and show that the relative peak area of Hg, Cd, and Zn increased with the increasing input voltage in the range of 50–90 V and then followed by a plateau at higher input voltage, indicating the microplasma capacity is sufficient for providing high vapor generation efficiency at 90 V. Thus, an input voltage of 90 V (output voltage of 2.6 kV) was used for subsequent experiments. The effect of the discharge voltage of PD-OES on the responses of Hg, Cd, and Zn were shown in Fig. S6e. The relative peak area of Hg, Cd and Zn increased significantly with increasing input voltage in the range of 50–80 kV followed by a stable trend or decreased at the higher voltage because the discharge became unstable when the voltage was too high. Finally, 90 V (output voltage of 2.6 kV) input voltage was selected as the optimal voltage.

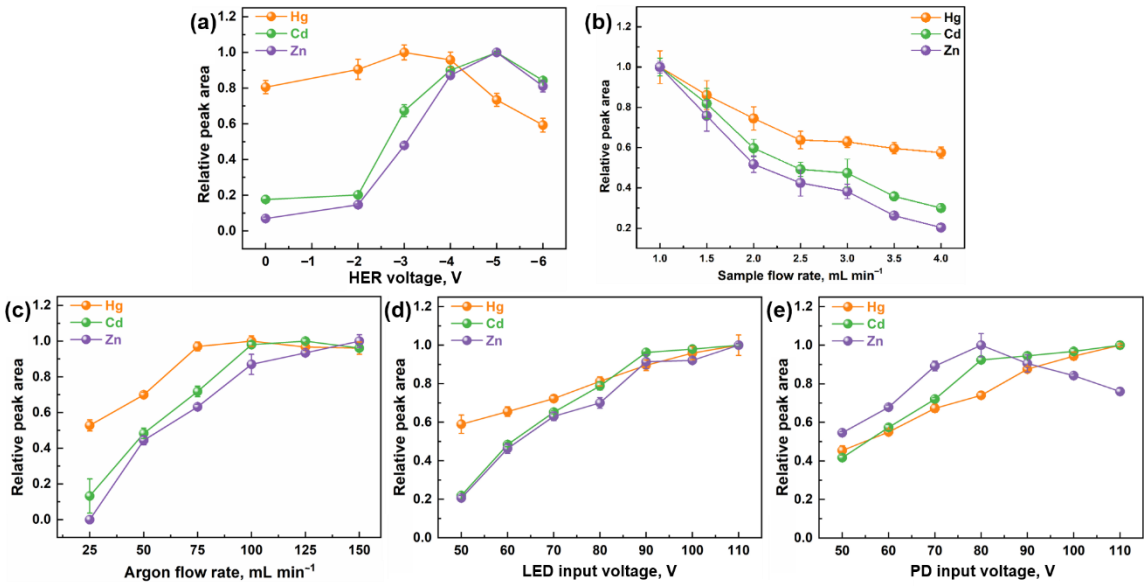

Figure. S6. Effect of (a) HER voltage, (b) sample flow rate, (c) carrier gas flow rate, (d) LED input voltage, and (e) PD input voltage in the HER-LED-μPIVG-μPD-OES system on the responses from 50 μg L^{-1} of Hg, 100 μg L^{-1} of Cd, and 200 μg L^{-1} of Zn.

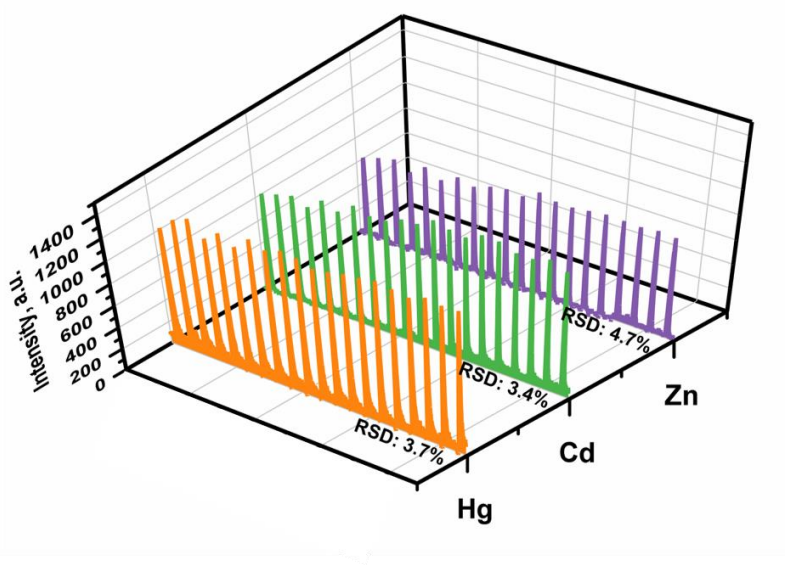

Figure. S7. Atomic emission signal profile of 20 consecutive measurements of 100 µg L^{-1} Hg, 200 µg L^{-1} Cd, and 200 µg L^{-1} Zn.

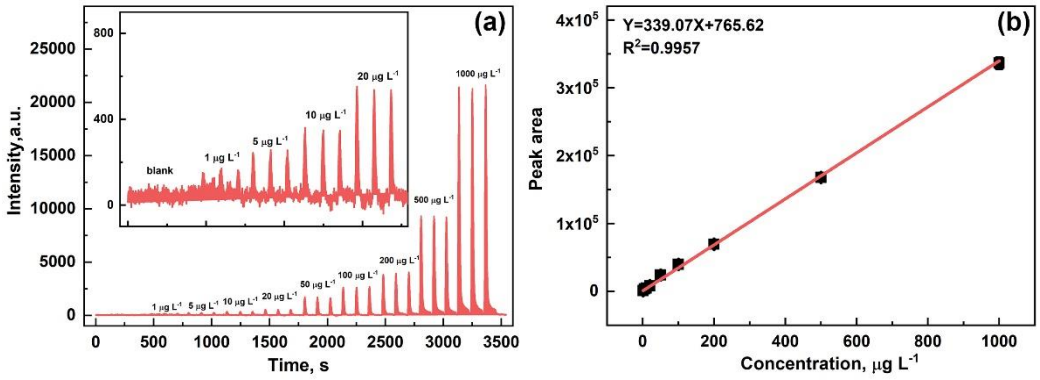

Figure. S8. Atomic emission signal profile and a calibration curve of Hg established by using HER-LED-μPIVG-μPD-OES with 1% formic acid.

Table S1. Effect of coexistence ions on the response of Hg, Cd, and Zn

Coexisting ions	Concentration, mg L^{-1}	Recovery, %		
		Hg	Cd	Zn
Fe^{3+}	10	85.5 ± 1.1	99.7 ± 0.4	99.8 ± 3.0
Co^{2+}	10	107.5 ± 3.6	97.6 ± 0.6	100.6 ± 3.0
Ni^{2+}	10	106.3 ± 3.0	96.6 ± 4.8	95.8 ± 4.1
Cu^{2+}	10	109.0 ± 3.0	100.8 ± 3.9	96.1 ± 6.0
Pb^{2+}	10	119.4 ± 1.5	104.0 ± 0.7	98.8 ± 3.1
K^{+}	10	105.8 ± 2.2	107.5 ± 1.8	102.6 ± 4.7
Ca^{2+}	10	93.7 ± 1.0	100.5 ± 2.6	87.4 ± 0.7
Mg^{2+}	10	94.3 ± 3.1	93.9 ± 11.3	97.5 ± 2.6
Na^{+}	10	101.2 ± 4.5	112.7 ± 5.4	107.8 ± 0.3
NO_3^{-}	10	108.8 ± 3.8	92.9 ± 4.0	86.3 ± 3.7
Cl^{-}	10	99.0 ± 1.9	90.7 ± 3.5	101.1 ± 1.6

A standard solution containing 50 μg L^{-1} Hg^{2+}, 100 μg L^{-1} Cd^{2+}, and 200 μg L^{-1} Zn^{2+} was used.

Table S2. Analytical Figures of Merit in Comparison with Other Similar Methods

Methods	LOD, µg L^{-1}			Ref.
	Hg	Cd	Zn	
SCGD-OES	349	9	42	[11]
dc-APGD-OES	–	50	100	[12]
DBD-OES	10	1.5	22	[13]
SCGD-OES	253	33	60	[14]
FLA-APGD	0.7	0.04	0.45	[15]
SAGD-AES	–	0.05	0.14	[16]
LED-µPIVG-AFS	0.007	0.05	0.5	[10]
PN-APGD-OES	-	45.9	48.9	[17]
MD-APGD-OES	-	5.9	0.61	[17]
This work	**0.8**	**10**	**14**	

SCGD: solution cathode glow discharge, dc-APGD: direct current atmospheric pressure glow discharge, DBD: dielectric barrier discharge, FLA: flowing liquid anode, SAGD: solution anode glow discharge, PN: pneumatic nebulization, MD: membrane desolvation.

References

1. N. Jiang, B. You, M. L. Sheng, and Y. J. Sun, *Angew. Chem. Int. Ed.*, 2015, **54**, 6251–6254. https://doi.org/10.1002/anie.201501616
2. M. M. Wei, L. M. Yang, L. L. Wang, T. Liu, C. B. Liu, Y. H. Tang, and S. L. Luo, *Chem. Phys. Lett.*, 2017, **681**, 90–94. https://doi.org/10.1016/j.cplett.2017.05.060
3. A. P. Grosvenor, S. D. Wik, R. G. Cavell, and A. Mar, *Inorg. Chem.*, 2005, **44**, 8988–8998. 10.1021/ic051004d
4. L. L. Ji, J. Y. Wang, X. Teng, T. J. Meyer, and Z. F. Chen, *ACS Catal.*, 2020, **10**, 412–419. 10.1021/acscatal.9b03623
5. H. Li, P. F. Yang, D. S. Chu, and H. X. Li, *Appl. Catal. A: Gen.*, 2007, **325**, 34–40. https://doi.org/10.1016/j.apcata.2007.02.007
6. F. H. Saadi, A. I. Carim, E. Verlage, J. C. Hemminger, N. S. Lewis, and M. P. Soriaga, *J. Phys. Chem. C*, 2014, **118**, 29294–29300. 10.1021/jp5054452
7. Z. L. Zhu, Q. J. Wu, Z. F. Liu, L. Liu, H. T. Zheng, and S. H. Hu, *Anal. Chem.*, 2013, **85**, 4150–4156. https://doi.org/10.1021/ac400368h
8. Z. A. Li, Q. Tan, X. D. Hou, K. L. Xu, and C. B. Zheng, *Anal. Chem.*, 2014, **86**, 12093–12099. https://doi.org/10.1021/ac502911p
9. Z. Wang, X. Wang, Q. Wang, X. Xiong, H. Luo, and K. Huang, *Microchem. J.*, 2019, **149**, 104052. https://doi.org/10.1016/j.microc.2019.104052
10. X. M. Pan, Y. Lin, Y. B. Su, J. H. Yang, L. B. He, Y. R. Deng, X. D. Hou, and C. B. Zheng, *Anal. Chem.*, 2021, **93**, 8257–8264. https://doi.org/10.1021/acs.analchem.1c01091

11. M. R. Webb, F. J. Andrade, G. Gamez, R. McCrindle, and G. M. Hieftje, *J. Anal. At. Spectrom.*, 2005, **20**, 1218–1225. 10.1039/B503961D

12. P. Jamróz, P. Pohl, and W. Żyrnicki, *J. Anal. At. Spectrom.*, 2012, **27**, 1032–1037. 10.1039/C2JA30017F

13. Y. Cai, X. G. Gao, Z. N. Ji, Y. L. Yu, and J. H. Wang, *Analyst*, 2018, **143**, 930–935. 10.1039/C7AN01633F

14. X. X. Peng, X. H. Guo, F. Ge, and Z. Wang, *J. Anal. At. Spectrom.*, 2019, **34**, 394–400. https://doi.org/10.1039/C8JA00369F

15. K. Greda, K. Swiderski, P. Jamroz, and P. Pohl, *Anal. Chem.*, 2016, **88**, 8812–8820. https://doi.org/10.1021/acs.analchem.6b02250

16. X. Liu, Z. L. Zhu, D. He, H. T. Zheng, Y. Q. Gan, N. Stanley Belshaw, S. H. Hu, and Y. X. Wang, *J. Anal. At. Spectrom.*, 2016, **31**, 1089–1096. https://doi.org/10.1039/C6JA00017G

17. J. H. Dong, C. Yang, D. He, H. T. Zheng, S. H. Hu, and Z. L. Zhu, *At. Spectrosc.*, 2020, **41**, 57−63.